

Numerical Modeling for Tunnel Lining Optimization

Jose Francisco Suárez-Fino *  and Juan M. Mayoral *

Geotechnical Department, Institute of Engineering, National Autonomous University of Mexico, Mexico City 04510, Mexico

* Correspondence: jfsuarezfino@consultecingenieria.mx (J.F.S.-F.); jmayoralv@ingen.unam.mx (J.M.M.)

Abstract: The construction of tunnels excavated by the conventional method in densely populated urban environments requires an adequate characterization of the loads acting on the primary lining during the excavation process, to ensure that the ground is deformed and stresses around the tunnel are relieved, simultaneously complying with the failure and serviceability limits of international standards while minimizing damage to nearby structures. In this paper, common lining design criteria are revisited, through the numerical simulation of an instrumented tunnel section which is part of a 4.5 km long metro line currently under construction in Mexico City. Key needs for improvement in current design approaches are identified. The tunnel was instrumented with load cells, extensometers, and topographical references for convergences and divergences. A three-dimensional finite difference model of the instrumented section was developed, and the load transfer mechanisms between the excavated soil and the primary lining were analyzed. Then, the numerical simulation of the contribution of the secondary lining in the overall stability for sustained load was established, along with the expected ground settlements, which can significantly affect nearby structures. Results gathered from this research are key for updating lining design criteria for urban tunnels built in stiff brittle soils.

Keywords: tunnel; numerical modeling; primary lining; optimization primary lining; load-transfer mechanism; conventional excavation; back-analyses; FLAC^{3D}



Citation: Suárez-Fino, J.F.; Mayoral, J.M. Numerical Modeling for Tunnel Lining Optimization. *Appl. Sci.* **2024**, *14*, 7415. <https://doi.org/10.3390/app14167415>

Academic Editor: Norhazilan Md Noor

Received: 10 July 2024

Revised: 4 August 2024

Accepted: 8 August 2024

Published: 22 August 2024



Copyright: © 2024 by the authors. Licensee MDPI, Basel, Switzerland. This article is an open access article distributed under the terms and conditions of the Creative Commons Attribution (CC BY) license (<https://creativecommons.org/licenses/by/4.0/>).

1. Introduction

As established by Mayoral et al. [1,2], modern tunnel design in densely populated areas, such as Mexico City, requires revising both state limits of failure (i.e., factors of safety for tunnel face and general stability) and service (i.e., ground deformations in the proximity of the tunnel at surface and within the tunnel) simultaneously, to avoid potential catastrophic collapse [3–6], or damage in nearby structures related to differential settlements [2,7–10]. This is particularly important when excavating with the conventional tunneling, CT, method [11], in heavily populated urban areas.

A key design issue that strongly controls both state limits is the soil–tunnel lining interaction, which is mostly a function of the tunnel cross-section geometry, lining thickness, structural configuration (i.e., one or two linings comprised for instance of shotcrete, reinforced concrete, steel frames), and recommended advancement length.

Several analytically derived approaches are available in the technical literature to study soil–tunnel lining interaction, ranging from conventional methodologies, based on the pressure of loose ground [12–15], relative stiffness solution [16], characteristics ground curves [17–20], support reaction curves [21–23], and longitudinal displacement curves, LDP, [24,25]. Recently, more sophisticated approaches using numerical modeling of the coupled soil–tunnel lining interaction are also employed [1,26–33].

Although several researchers have attempted to study the soil–tunnel lining interaction through instrumentation of actual tunnels [34–36] and centrifuge test models [37–39], to date, there is still a lack of information regarding the soil–lining interaction during

conventional tunneling in stiff cemented soils, which, in turn, is needed to assess the validity and areas of improvement of current design methodologies.

This paper presents an in-depth study, using numerical modeling and instrumentation, of the soil–tunnel lining interaction in a tunnel during conventional excavation, aiming at assessing the lining performance while seeking potential optimization of the lining thickness. The tunnel is part of a metro extension currently under construction in Mexico City. The results gathered were compared with those estimated using some of the most used analytical conventional design methods, to identify their main limitations. Finally, once the proposed approach was validated, the efficiency of different lining alternatives was revised according to the global tunnel performance, considering both composite lining (i.e., primary and secondary lining) and single lining, establishing an optimal tunnel lining design for the case studied.

2. Case Study

The studied case was presented by Mayoral et al. [40] and consisted of a 10 m-diameter shallow urban tunnel, 4.5 km long, currently under construction in the western portion of Mexico City. Figure 1 depicts the location of the project along with the Mexico City geotechnical zoning map. Although the instrumented metro line crosses all the geotechnical zones found in the city, the results presented here only pertain to the portion of the tunnel found at Zone I, mostly within the so-called Tarango formation. This formation is composed predominantly of highly cemented silty sands and dense to very dense sandy silts with varying degrees of cementation. Thus, shear strength and compressibility parameters varied widely. Furthermore, in this zone, cavities, caverns, and old tunnels excavated for mining, as well as uncontrolled fillings, are often present. These facts directly impact the tunneling process.

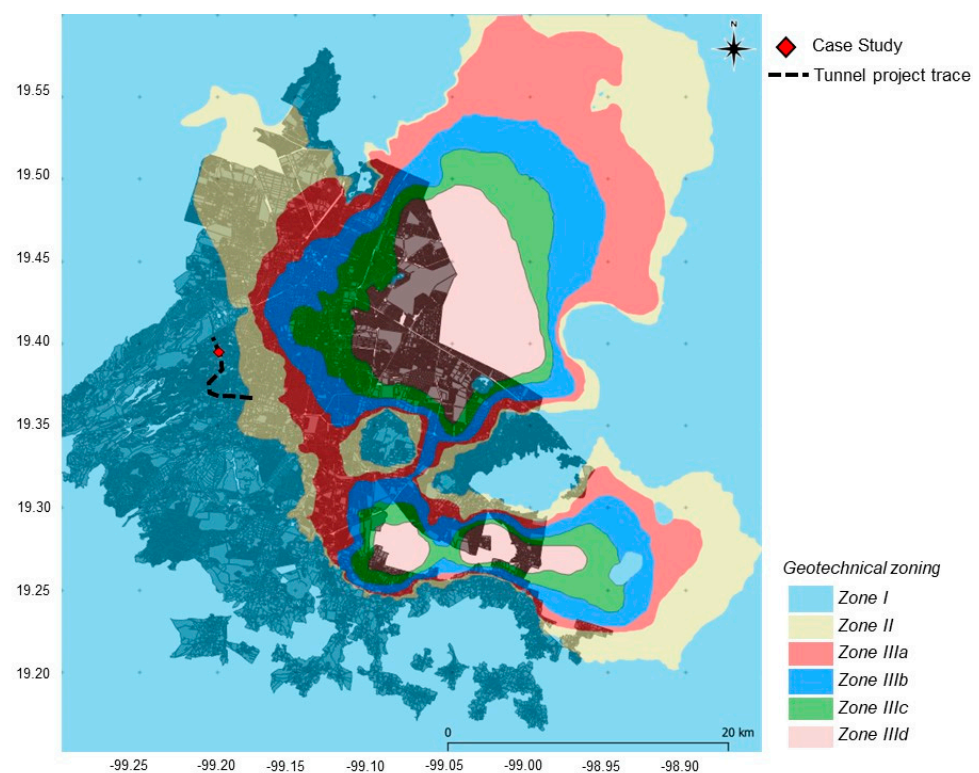


Figure 1. Project trace and geotechnical zoning of Mexico City.

2.1. Geotechnical Conditions

Four standard penetration tests SP-1, SP-2, SP-3, and SP-4 were conducted at the site to characterize the subsurface conditions. The average exploration depth was around 40 m.

In addition, index properties were obtained from disturbed samples retrieved at several depths, which were used to establish the geotechnical units according to the Unified Soil Classification System (USCS). Strength and deformability parameters were determined from unconfined compression tests and triaxial UU tests conducted in undisturbed samples, as well as in situ phicometer and pressuremeter tests. Figure 2 shows the soil profile characterization. In addition, empirical correlations [41] based on SPT blow counts (N_{SPT} values) were also used to determine strength and deformability parameters (i.e., cohesion c , internal friction angle φ , and Young’s modulus at 50% strain E_{50}). In the cases where N_{SPT} values were larger than 50, the values used in the correlation were extrapolated according to the LRFD Bridge Design Specifications [42] AASHTO (Equation (1)).

$$N_{SPT} = \frac{(50 + N_2) \times 30}{15 + N_3} \tag{1}$$

where N_{SPT} is the extrapolated number of standard penetration test blow counts and N_2 and N_3 are the second and third advances of the standard penetration test.

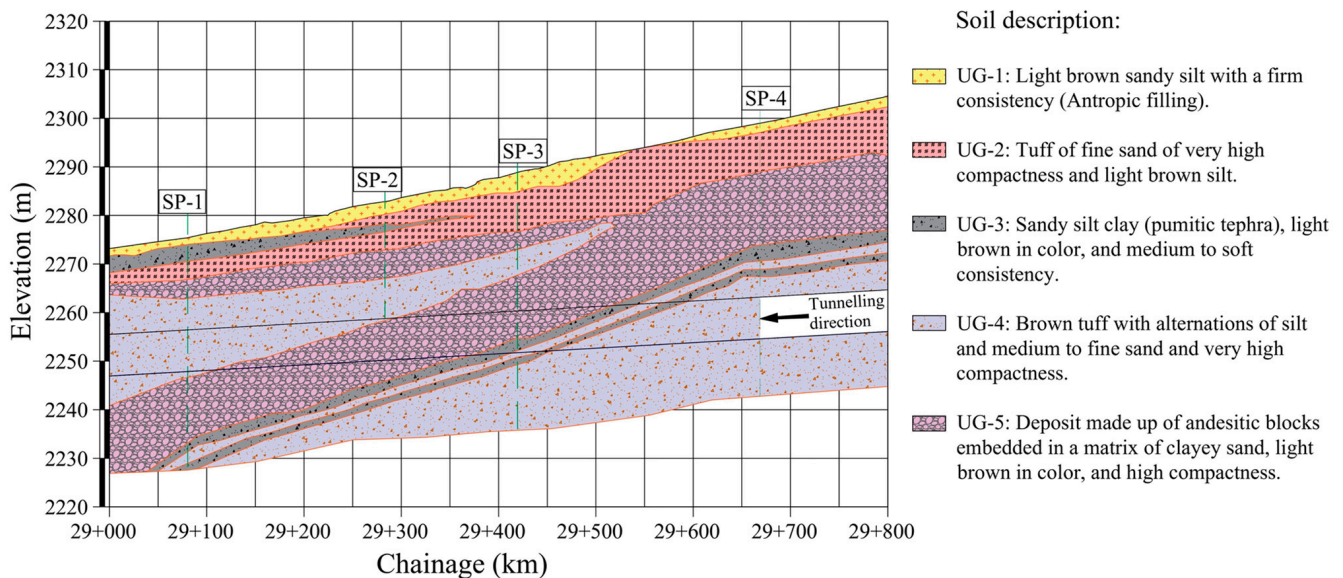


Figure 2. Soil profile and tunnel at the studied site.

The geotechnical properties of the soil profile estimated initially are summarized in Table 1. Poisson’s ratio ν was defined from typical values for similar materials. The water table was not detected until the maximum explored depth.

Table 1. Initial geotechnical properties at the studied site estimated with correlations.

Layer	USCS	N_{SPT} (Blows Counts)	γ (kN/m ³)	c (kPa)	φ (°)	E_{50} (MPa)	ν (-)
UG-1	ML	42	15.8	18	28	120.8	0.32
UG-2	SM	167	18.2	45	29	900.4	0.28
UG-3	CL-ML	40	17	13	27	97.5	0.34
UG-4	ML	126	18.2	40	28	470.5	0.28
UG-5	SC	80	19.2	33	31	303.2	0.27

N_{SPT} = extrapolated number of standard penetration test blow counts; γ = unit weight; c = cohesion; φ = friction angle; E_{50} = Young’s modulus at 50% strain; ν = Poisson ratio.

2.2. Tunnel Geometry and Excavation Process

The tunnel geometry is shown in Figure 3. It was projected to have an external width of 10.60 m and an external height of 8.50 m. The construction sequence considers three partial excavations: (1) upper-middle section, (2) central bench, and (3) lateral benches alternately. The primary lining, PL, comprises a 20 cm thick layer of steel fiber-reinforced shotcrete (SFERS), $f'_c = 25$ MPa. The secondary lining, SL, consisted of a 40 cm thick reinforced concrete support with design strength after 28 days of f'_c , 30 MPa.

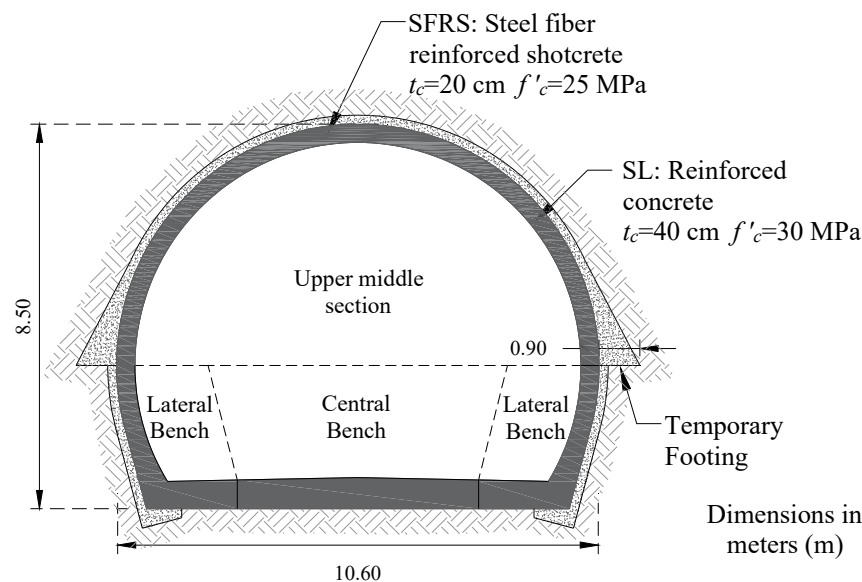


Figure 3. Tunnel cross-section and primary lining configuration used.

A schematic representation of the tunnel excavation process is depicted in Figure 4, consisting of four main stages: (1) excavation of the upper-middle section with excavation phase lengths of 1.0 m stabilizing the ground through the primary lining, leaving a central pillar unexcavated to reduce the risk of tunnel face failure; (2) once an excavation length of the upper-middle section of 35 m has been reached, the excavation of the central bench begins (stage 2); first, a 9 m long work ramp is built and behind it, the central bench is completed; (3) when a distance of 35 m of excavation of the central bench is reached, measured from the beginning of the ramp, the alternate excavation of the lateral banks with advances of 3.0 m is started, stabilizing them by employing a 20 cm thick layer of shotcrete reinforced with steel fibers; and (4) reinforcement and casting of the footings and sidewalls of the secondary tunnel lining, having an advance of 20 m; the secondary lining of reinforced concrete is implemented in the vault. Simultaneously, the reinforcement and casting of the bottom slab are carried out to close the tunnel ring. Figure 5 shows the excavation of the upper half of the section complete with the central core, highlighting the adverse ground conditions; poor soil quality and the presence of water seepage are observed.

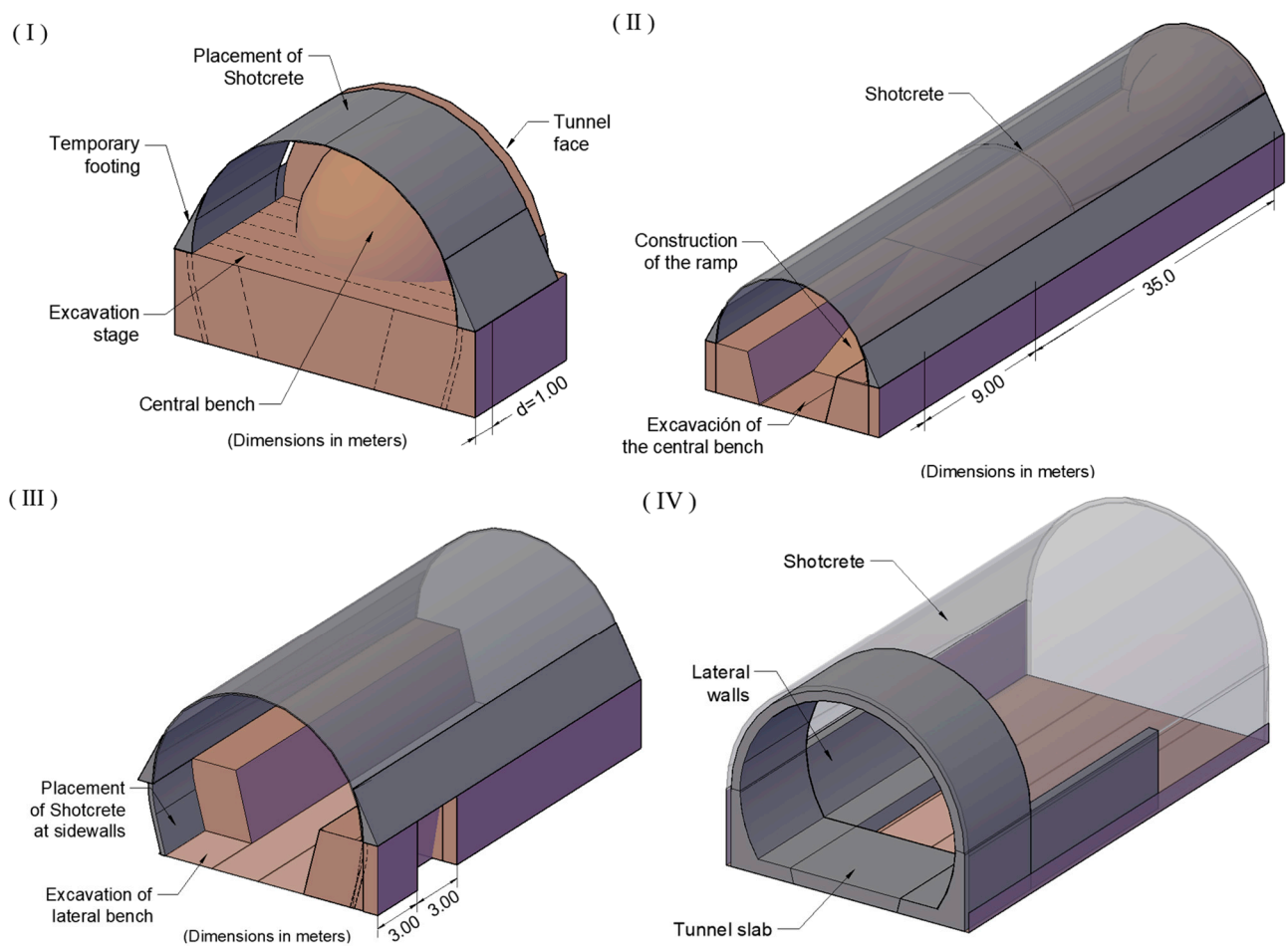


Figure 4. Schematic tunneling process [29]. (I) Stage 1, (II) Stage 2, (III) Stage 3, and (IV) Stage 4.



Figure 5. Excavation of the complete upper half section with a central core. It shows the poor quality of the soil and the presence of water seepage.

3. Tunnel Instrumentation

Six convergence measurement stations (EM-7, EM-6, EM-5, EM-4, EM-3, EM-2, and EM-1) were installed, each with three measurement lines (L1, L2, and L3), and topographic references. In addition, at EM-4, a rod extensometer, three radial pressure cells and two tangential pressure cells were also deployed at this control section, as shown in Figure 6 and Table 2.

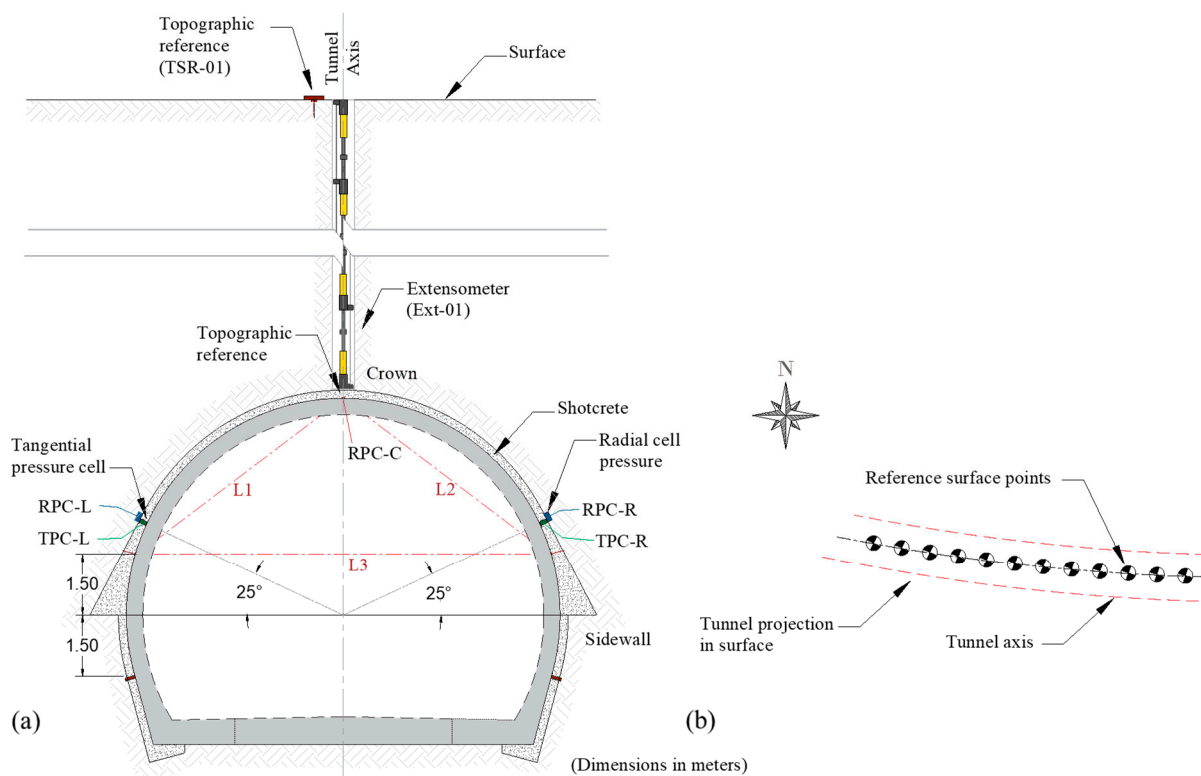


Figure 6. Schematic representation of the tunnel instrumentation: (a) inside the tunnel and (b) topographical elevation survey references, modified from [29].

Table 2. Instrumentation sensors and variables measured.

Sensor ID	Instrumentation	Variables Measured
L1, L2 and L3	Convergences and divergences	Tunnel distortion
TSR-01	Reference surface points	Surface settlements
Ext-01	Extensometer	Tunnel crown settlements
RPC-L, RPC-R and RPC-C	Radial pressure cells	Radial stress on primary lining
TPC-L and TPC-R	Tangential pressure cells	Axial stress on primary lining

Stations EM-5, EM-6, and EM-7 were installed at 5 m, 10 m, and 20 m upstream of the control section (EM-4), respectively. Stations EM-3, EM-2, and EM-1 were located at 5 m, 10 m, and 20 m downstream of the control section (EM-4), respectively.

These measurements were complemented with reference surface points to monitor the settlements along the tunnel axis. In addition, a tunnel section (29+300) was instrumented with one extensometer, radial, and tangential pressure cells to establish the load acting on the PL. First, an extensometer was installed before the excavation face reached the instrumented section. Then, radial pressure cells (RPCs) were installed between the ground and the shotcrete of the primary lining (SFRC) to measure the radial stress, and tangential pressure cells (TPCs) were embedded within the shotcrete to measure the axial stresses. Figure 6b shows the configuration of the reference surface points installed to monitor the settlements along the tunnel axis. A topographical survey of both the primary and secondary lining was carried out to establish convergences and divergences. Table 2 presents a summary of the installed sensors.

To ensure proper contact between the soil and the radial and tangent load cells, prior to the placement of the shotcrete reinforced with fibers, the soil surface was smoothed out

with a thin layer of mortar at the interface between the instruments and the soil, according to the following procedure:

1. Preparation of the installation area:

Cleaning was carried out, removing loose material and dust from the surface where the pressure cells were installed. Subsequently, the ground surface was smoothed, using a mortar to obtain a uniform surface to ensure optimal contact with the load cells.

2. Marking of the location:

The specific points where the radial and tangential pressure cells were installed were marked.

3. Drilling and hole preparation to fix the load cells to the soil:

Hole drilling on the ground was carried out at the marked locations to place the load cells. Subsequently, the holes were cleaned to ensure that they were free of obstructions, to allow an accurate installation of the sensors.

4. Installation of the cells:

The load cells were placed, ensuring that they were correctly oriented to measure radial and tangential pressures. Subsequently, the area around the cells was sealed with concrete mortar to protect and fix the sensors.

5. Instrumentation connection:

Once installed, the cells were connected with flexible cables to the data acquisition system (Datalogger), ensuring that the connections were well protected with a flexible polyduct and sealed against humidity, using a special tape.

6. Testing and Calibration:

Initial tests were carried out to verify that the cells were working properly and that the readings were consistent. Finally, cell calibration was carried out according to the manufacturer's specifications to ensure measurement accuracy.

The following Figures 7–11 show photographs of the installation and measurement of the instruments.



Figure 7. Drilling for the installation of the extensometer and measurement of the instrument. Photographs taken by the author, 2021.

The pressure transducers are not protected with steel conduits, but with a flexible plastic polyduct and a special tape to prevent ruptures, to ensure the accuracy of the measurements. Finally, Figure 12 shows the installation of the instruments to the Datalogger and the first reading of each of the instruments installed in the primary lining.



Figure 8. Measurement of convergences during the excavation of the upper half section. Photographs taken by the author, 2021.



Figure 9. Maneuvers during the instrumentation of radial cells. Photographs taken by the author, 2021.



Figure 10. Finally, the pressure transducers are protected with steel ducts and are channeled to the Datalogger where they are connected. Photographs taken by the author, 2021.



Figure 11. Placement of the first layer of shotcrete with 10 cm thick fibers, covering the periphery of the tunnel vault and the instrumented radial pressure cells. Photographs taken by the author, 2021.



Figure 12. Photograph showing the connection of the instruments to the Datalogger. Once connected, the first readings are taken on a laptop using the Logger Net software version 4.5.

Figure 13 shows the vertical ground movements measured with the extensometer at the tunnel keystone (tunnel crown) in the control section. It is observed that when the excavation face is 70 m from the control section, the settlement at the tunnel keystone tends to stabilize. It is interesting to note that, when starting the excavation of the bench at 35 m away, according to the construction procedure described above, the displacements increased up to 14 mm.

Figures 14–16 present the values measured at each convergence station placed before the control section, and Figures 17–20 present the values measured at the convergence stations placed after the control section. Figures 14–20 show the evolution of the ground deformation around the tunnel, recorded by the convergence measuring stations (EM) during the progress of the excavation. In general, it is observed that the tunnel walls tend to close, as indicated by line L3. It is interesting to note how, as the excavation front moves away, the deformations tend to stabilize until the benching process of the excavation begins, which causes a change in the deformation trend.

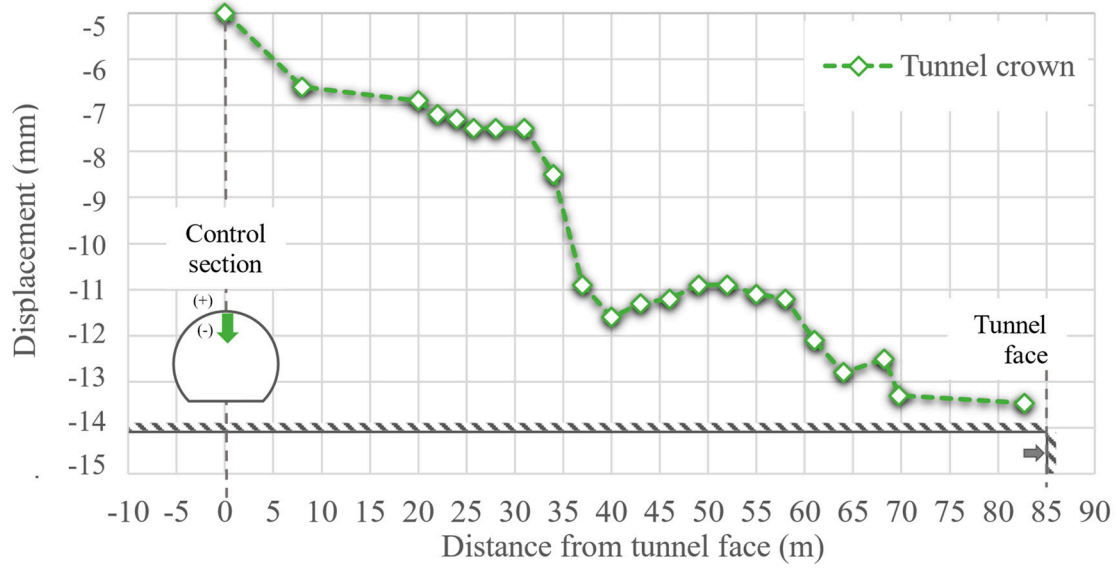


Figure 13. Measured vertical ground movements at the tunnel crown in the control section (the arrow indicates the tunnelling direction).

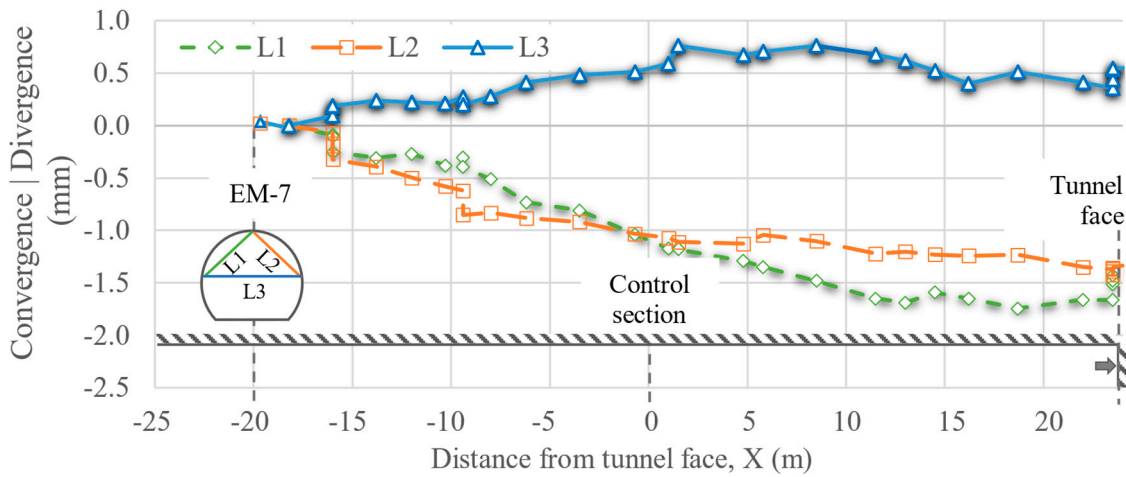


Figure 14. Convergences and divergences, EM-7, located 20 m before the control section.

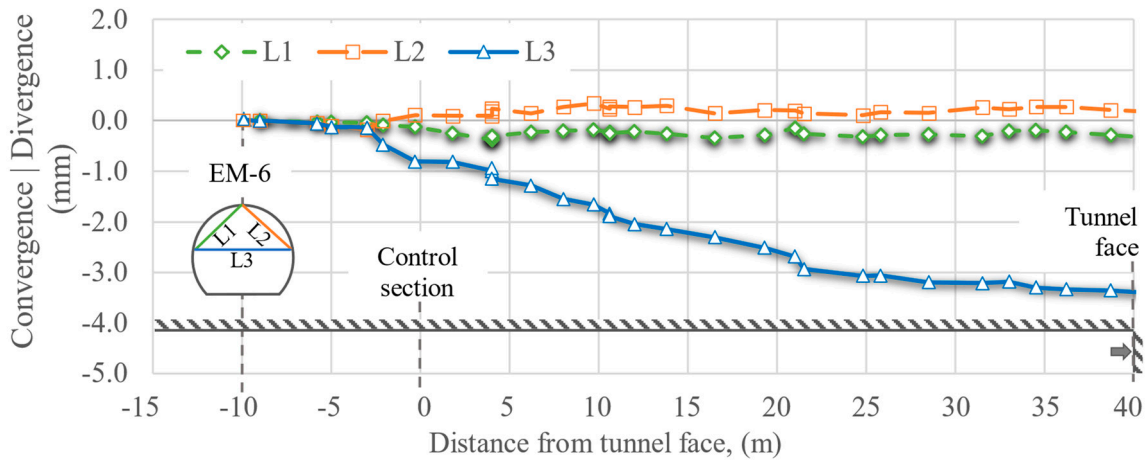


Figure 15. Convergences and divergences, EM-6, located 10 m before the control section.

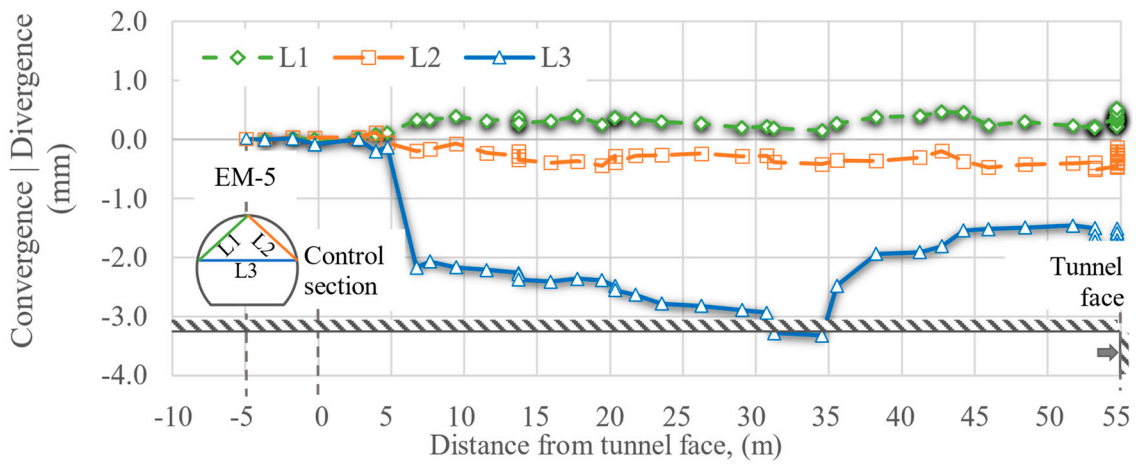


Figure 16. Convergences and divergences, EM-5, located 5 m before the control section.

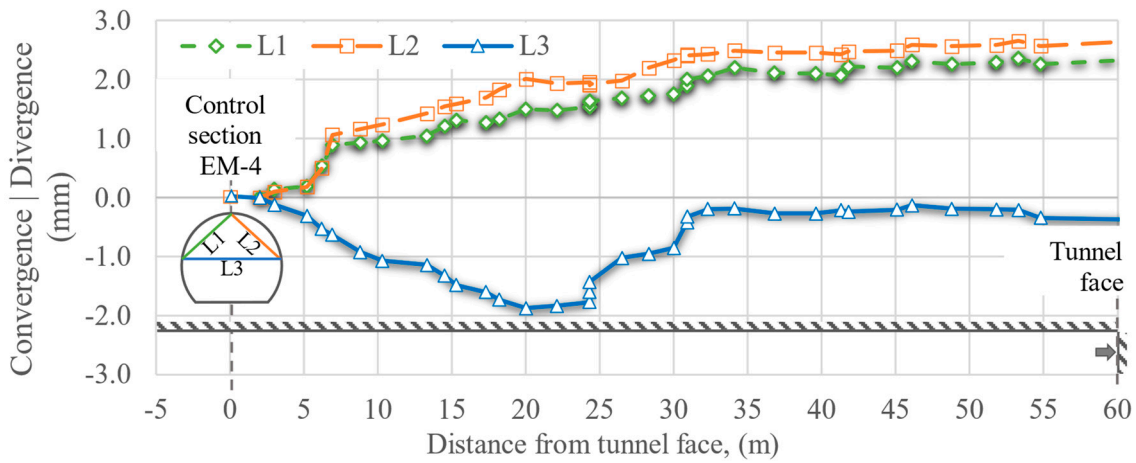


Figure 17. Convergences and divergences, EM-4, located at the control section.

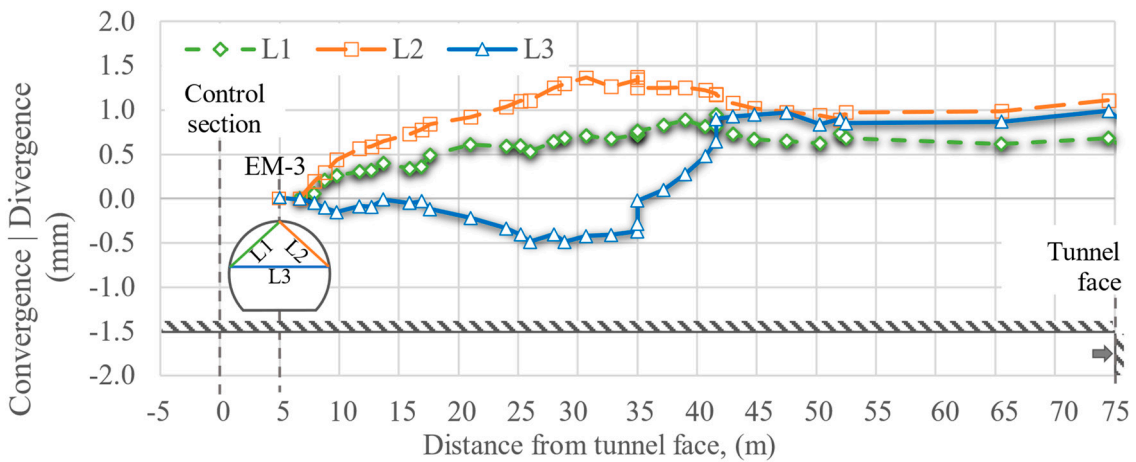


Figure 18. Convergences and divergences, EM-3, placed 5 m after the control section.

Similarly, the effect of the excavation on the settlement of the surface soil in the control section is quite low when the distance to the excavation face reaches 65 m (Figure 21). In the same figure, it is observed that 30 m before the excavation reaches the control section, no settlement develops. The settlement is triggered once the excavation starts, reaching 10 mm, and stabilizes at 65 m from the excavation face. A very similar response was recorded by the reference installed in the tunnel keystone, whose results are shown in Figure 13.

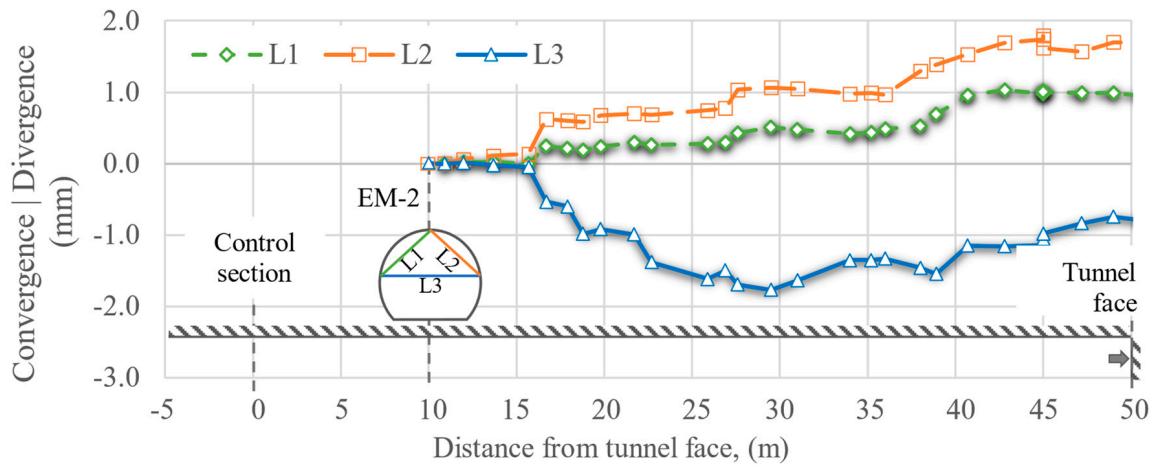


Figure 19. Convergences and divergences, EM-2, placed 10 m after the control section.

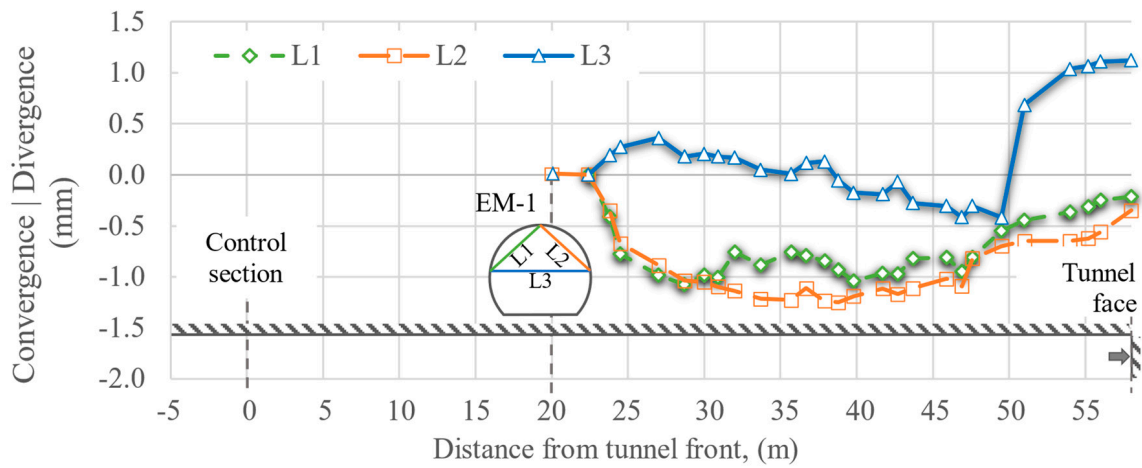


Figure 20. Convergences and divergences, EM-1, placed 20 m after the control section.

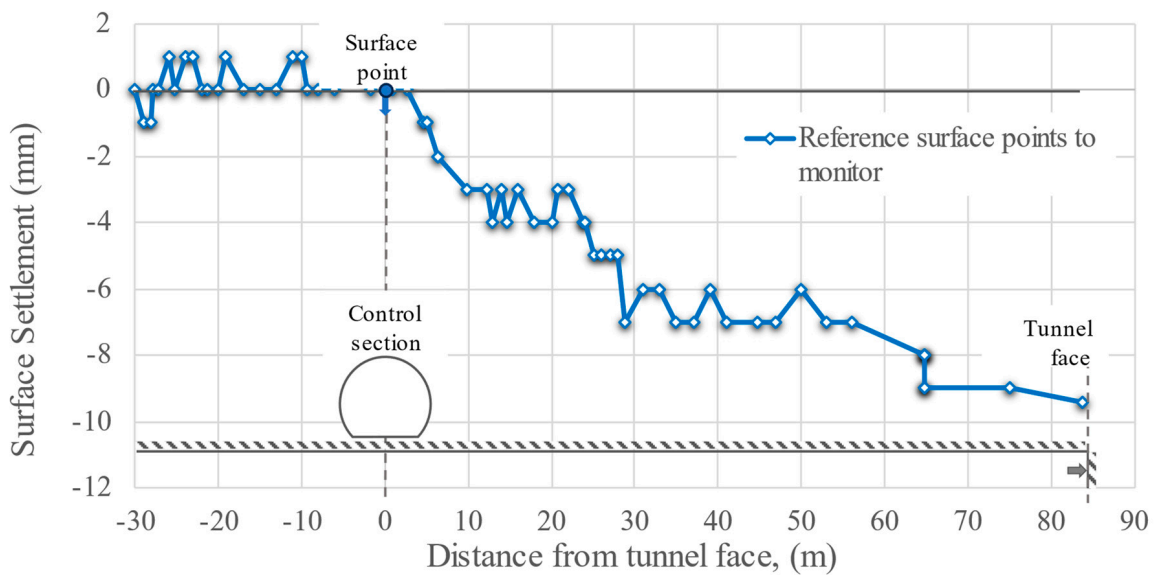


Figure 21. Surface points to monitor settlements in the control section.

Figure 22 shows the results of the extensometer measurements. It is observed that 25 m before the excavation face reaches the control section, there is no settlement. However, at 5 m from the excavation face, ground settlement begins to appear. By the time the excavation front passes through the control section, 5 mm of settlement has already accumulated, representing 35% of the total settlement of 14 mm.

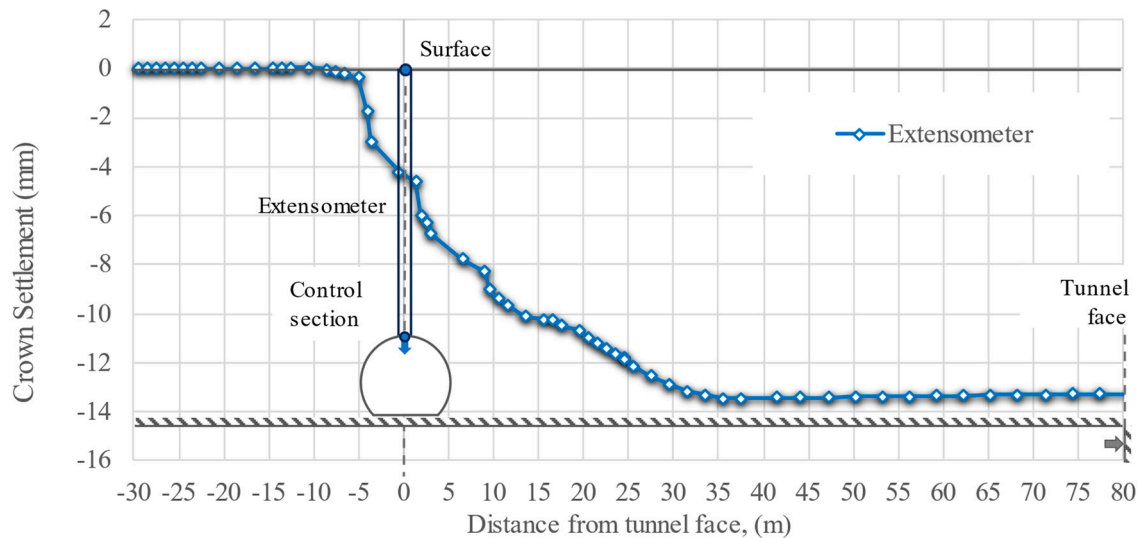


Figure 22. Extensometer measurements.

This behavior indicates that the ground begins to yield significantly shortly before the excavation front reaches it and continues to deform until it stabilizes after the excavation front is 65 m away from the control section.

The instrumentation with radial and tangential pressure cells was embedded in the support in radial and tangential directions in order to measure the actual stresses acting on the primary lining.

Figure 23 shows the history of the radial pressures recorded at the keystone and the tunnel walls. At the beginning of the excavation, the cells located in the gables recorded a sudden increase in shear stresses, reaching up to 60 kPa when the excavation face was 25 m from the control section. Subsequently, both cells continued to record an increase in stresses, reaching 80 and 90 kPa when the excavation face was 45 m away. The cell located at the keystone recorded a maximum of 45 kPa at 25 m, stabilizing at that value. This behavior is attributed to stress redistribution in the soil.

Figure 24 shows the history of the tangential pressures recorded on the tunnel walls. At the beginning of the excavation, both cells recorded a sudden increase in stresses, reaching 2.5 MPa when the excavation face was located 5 m from the control section. Subsequently, both cells continued to record an increase in stress, reaching 4 MPa when the excavation face was at 12 m, and remained almost constant thereafter.

In summary, the radial pressure cells showed a significant increase (up to 50%) in stresses during the early stages of excavation, indicating a redistribution of stresses in the ground. After the construction of the primary tunnel support, the stresses recorded by the radial and tangential cells stabilized, suggesting an improvement in tunnel stability prior to the construction of the secondary and permanent lining.

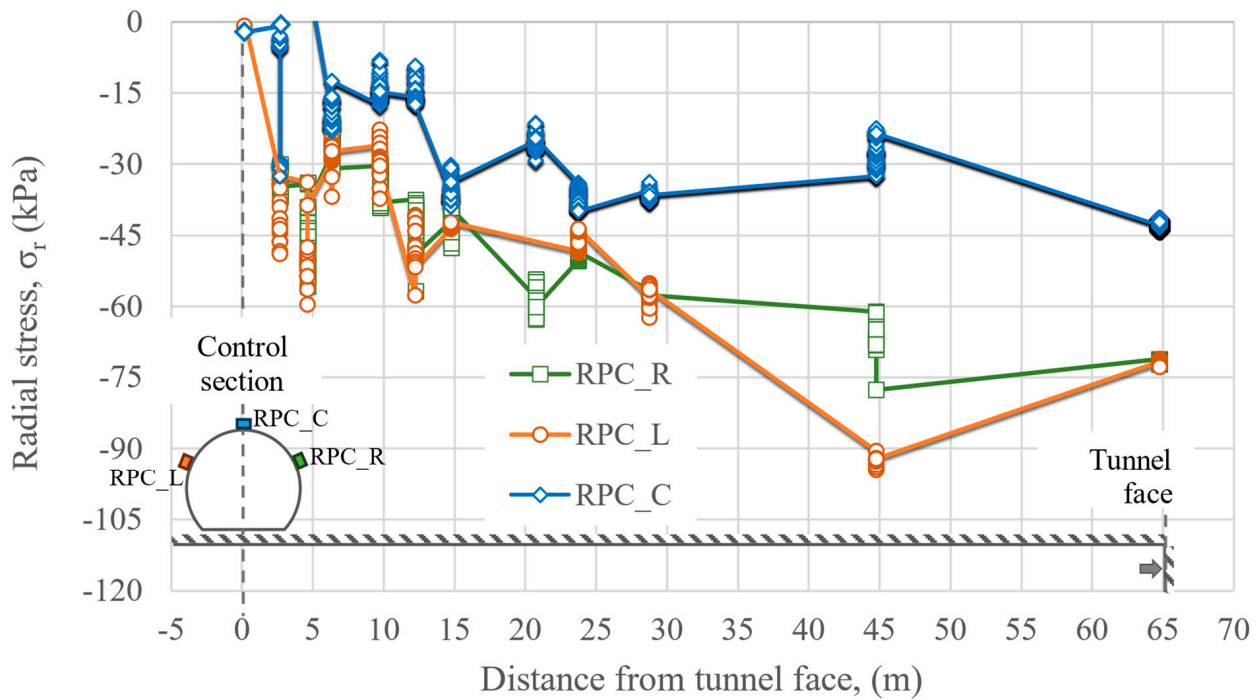


Figure 23. Recorded radial pressures.

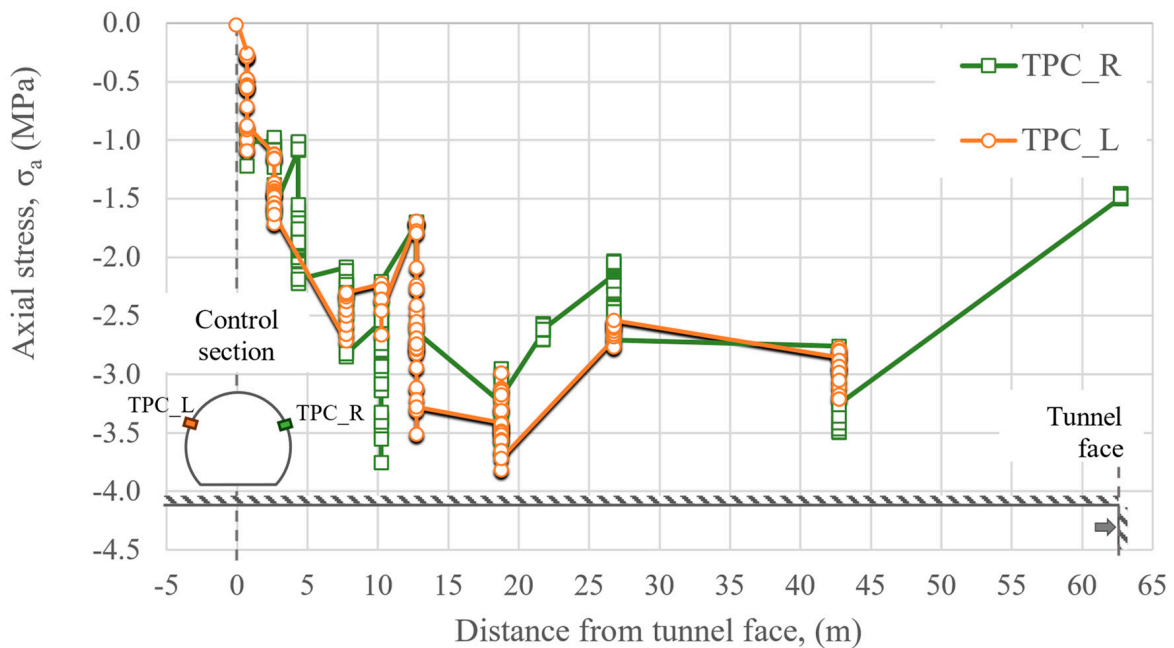


Figure 24. Recorded axial pressures.

4. Numerical Modelling

Three-dimensional finite difference numerical models were developed using the program FLAC3D v. 5.0. [43], as depicted in Figure 25, to assess the load transfer mechanism in the primary and secondary lining. To simulate soil behavior, it was deemed appropriate to consider an elasto-plastic Mohr–Coulomb model because of the expected low levels of soil non-linearities during the construction process, and the brittle stress–strain behavior exhibited by these cemented soils. The initial parameters considered are those shown in Table 1, and the soil profile was idealized horizontally according to the geotechnical layering prevailing at the instrumented tunnel section (i.e., chainage 29+350 and 29+250).

The model consists of 319,000 three-dimensional solid elements representing the soil mass through which the tunnel is excavated. Within the domain of the model, further refinement of the mesh was adopted on the periphery of the tunnel and in the established control section, where the elements have a dimension of 0.25 m on each side on average. Figure 25a shows the global model domain. Initially, the geo-static state of stress was determined in the soil mass by the application of a body force equal to the acceleration of gravity. As boundary conditions, only the vertical displacements were permitted on the lateral faces, and the base of the model was fixed in all directions. The modeling process consisted of the simulation of each excavation step, in which a null-type material [43] was used to represent the elements that were removed from the model. In the same way, the placement of the linings according to the construction process described previously was included in the modeling, for which SHELL elements were used to simulate the PL and the SL with solid elements. It is warranted to mention that a relaxation of the soil around the tunnel was allowed prior to placing the SHELL by solving the system of equilibrium in every excavation step to effectively simulate each advancement of the construction procedure. To simulate the PL behavior, a non-linear stress–strain relationship considering the evolution of shotcrete properties with time was used (see Figure 26). This consideration permits the relaxation of the soil (solid elements) in a more realistic way. Thus, the primary lining is flexible in the early stages and becomes stiffer as the excavation moves forward until reaching its design strength at 7 days, avoiding both the generation of spurious stress concentration in the lining and underestimation of the displacements. In the case of the SL, its behavior was simulated with a linear elastic model. Figure 25b shows the discretization of the mesh according to the excavation steps (upper-middle section, central bench, and lateral benches).

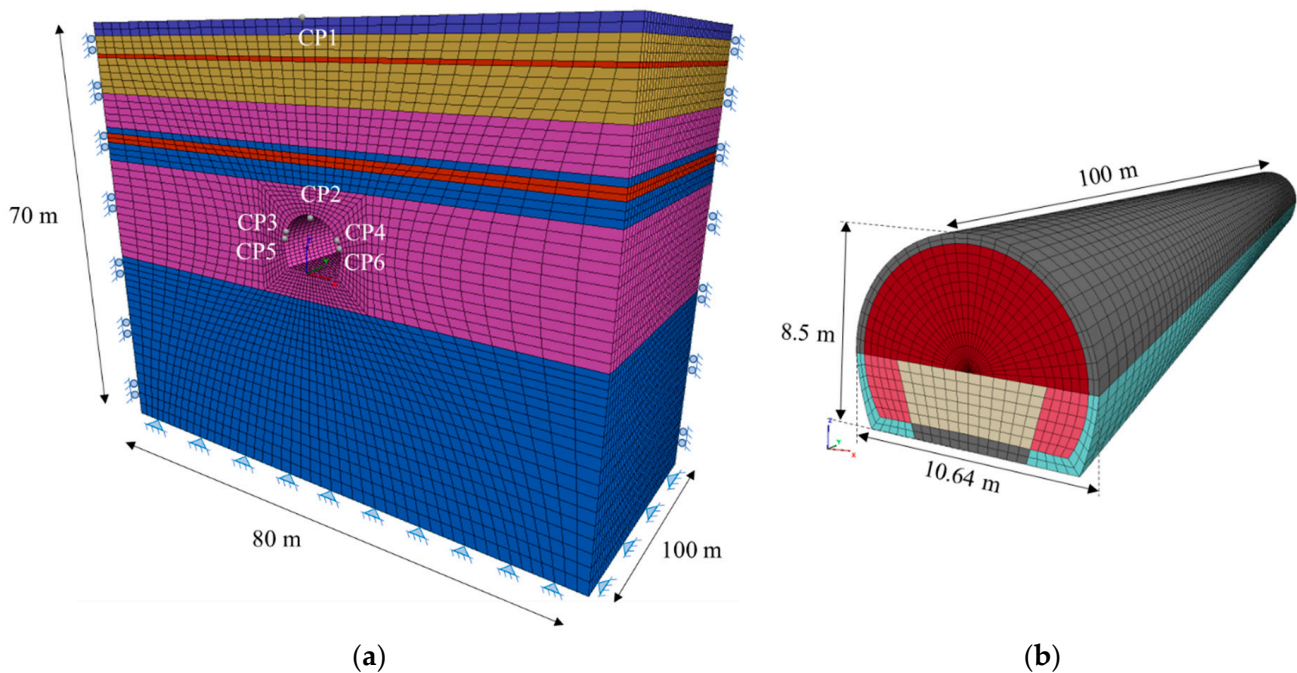


Figure 25. Three-dimensional mesh of finite differences: (a) global domain of the model; (b) discretization of construction stages.

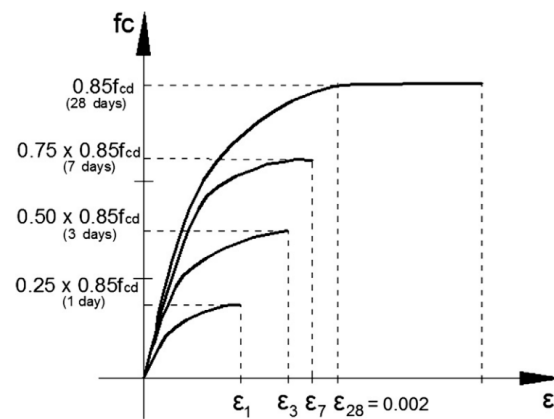


Figure 26. Evolution of SFRC stress–strength relationship over time.

Model Prediction and Back-Analyses

A blind model prediction and back-analyses were conducted to calibrate the numerical models of the analyzed section. Initially, the properties shown in Table 1 were used to assess the potential foreseen capability of the model, comparing the data gathered from the instrumentation (i.e., topographic references, tunnel cross-section converges and divergences, and radial and axial pressure cells) with those obtained in the control points placed in the numerical model, whose locations correspond to every instrument (see Figure 25a). In a second step, the soil properties were adjusted slightly to better match the measured response. If there was a discrepancy, Young’s modulus, cohesion, and friction angle were adjusted accordingly to account for changes associated with the excavation process at the soil adjacent to the excavation seeking to minimize the relative error.

This step was repeated until the relative error between the computed and measured values (i.e., surface and tunnel crown settlements, radial and axial stresses) were minimized. The final properties (i.e., obtained through the back-analysis) are also presented in Table 3.

Table 3. Back-calculated geotechnical properties at the studied site.

Layer	USCS	N _{SPT} (Blows Counts)	γ (kN/m ³)	c (kPa)	φ (°)	E ₅₀ (MPa)	ν (-)
UG-1	ML	51	15.8	20.5	28	160	0.32
UG-2	SM	167	18.2	51.2	30	970	0.28
UG-3	CL-ML	40	17	15.6	27	123	0.34
UG-4	ML	126	18.2	47.5	28	590	0.28
UG-5	SC	80	19.2	36.3	32	445	0.27

N_{SPT} = extrapolated number of standard penetration test blow counts; γ = unit weight; c = cohesion; φ = friction angle; E₅₀ = Young’s modulus at 50% strain; ν = Poisson ratio.

Figure 27 shows the displacement obtained from the numerical model and those measured at the surface with the topographic survey, along with the readings from the extensometer installed from the surface to the tunnel crown. It is warranted to notice that the ground deformation at the surface is around 1 mm at the instrumented section when the excavation reaches this location, whereas at the tunnel crown, it reaches 6 mm. For completeness, the blind model predictions, identified as FLAC_ini, were also included in all comparisons. After the excavation front passes by the instrumented section, an abrupt deformation of both the ground surface and tunnel crown is observed. This is associated with the brittle stress–strain relationship observed in cemented silty sand and sandy silts, as depicted in Figure 28, which summarizes the stress–strain curves obtained from unconfined compressions tests (UCTs) of the geomaterials found in the studied site.

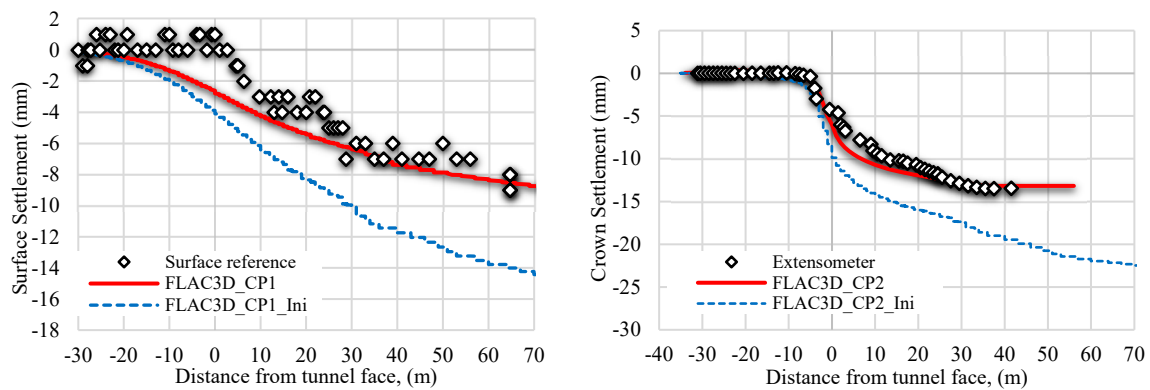


Figure 27. Settlements recorded and predicted on the surface above the tunnel axis and on the tunnel crown.

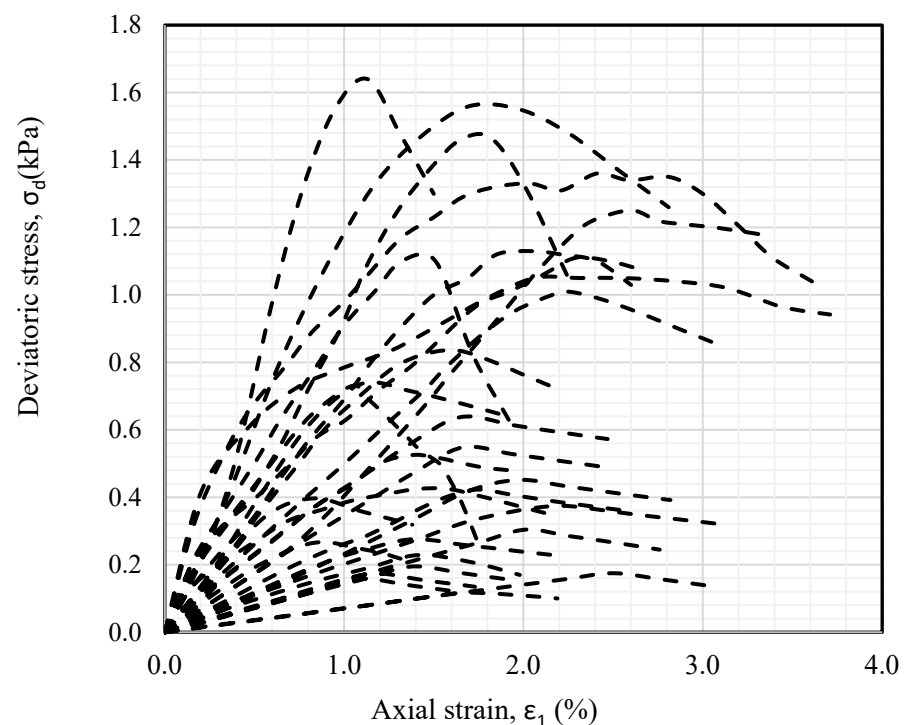


Figure 28. Unconfined compression test stress–strain relationship of the tuff soils.

Vertical and horizontal movements at the tunnel crown and sidewalls, respectively, are depicted in Figure 29. As can be seen, the results obtained with the numerical model are in good agreement with those gathered from the instrumentation, where a larger displacement was obtained at the tunnel crown with respect to the horizontal displacement measured at the sidewall, as expected.

Similarly, Figure 30 shows the pressures measured at TPC and RPC load cells located in the sidewall and the tunnel crown, and those computed with the numerical model; as can be seen, the model predictions are in good agreement with the measured response.

The measured and computed convergences at the secondary lining after its construction are shown in Figure 31. As can be noticed, there is a good agreement between the computed and measured responses. Thus, the numerical model is able to foresee the measured secondary lining performance very closely for all cases.

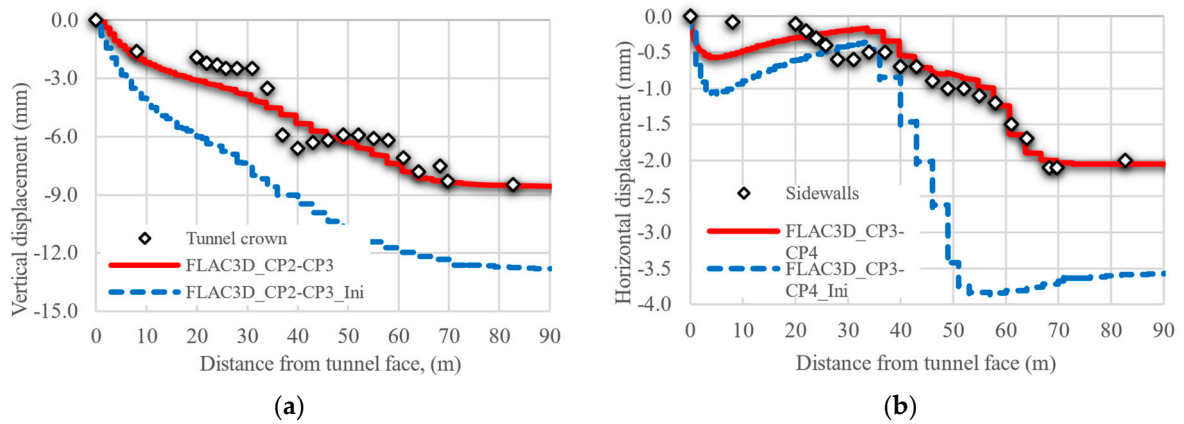


Figure 29. Measured and predicted ground movements at (a) tunnel crown and (b) sidewalls, respectively.

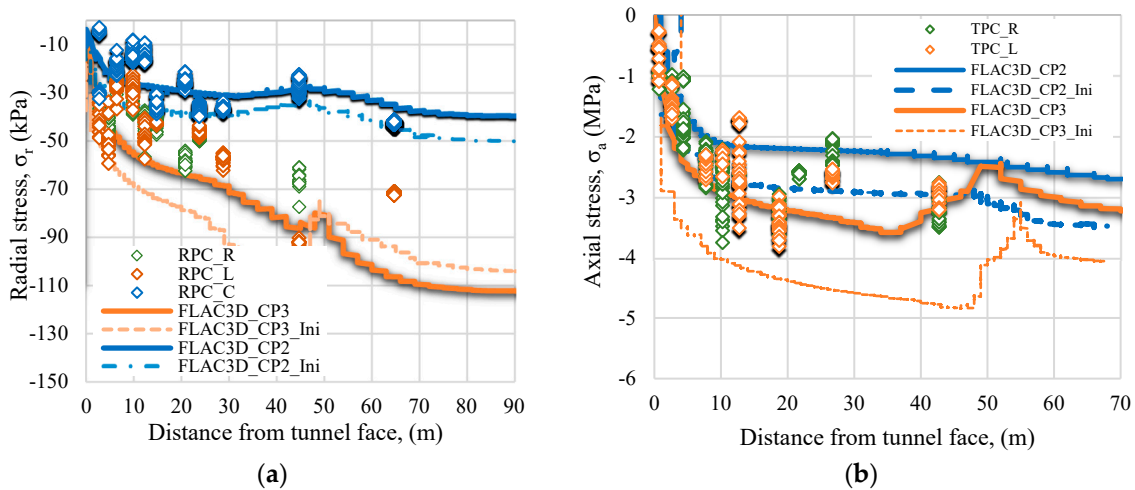


Figure 30. Pressures measured and predicted on the primary lining: (a) radial; (b) axial.

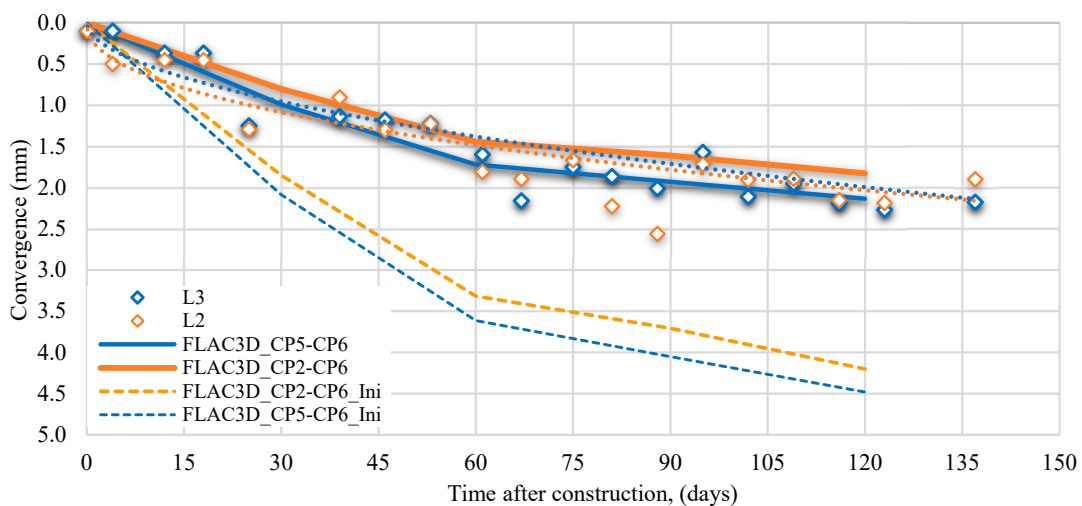


Figure 31. Measured and predicted convergences at the monitoring section in the secondary lining.

5. Comparison with Analytical Methods

Very often, simplified methods such as those based on the development of ground softening pressure on the tunnel vault [13,15] may lead to costly designs and unsafe scenarios

associated with this fact can potentially lead to structural damage to adjacent structures. In addition, in Figure 32a, the fitted curve from the calibrated numerical model exhibits a different behavior than the other proposed equations derived from several measured data [49], elastic analysis [44], and numerical models [25]. This behavior can be attributed to the idealized conditions considered to derive the equations to computed GRC and LDP (i.e., circular tunnel cross-section, and the assumption of $K_o = 1$). Figure 33 shows the displacement contours around the tunnel, considering the idealized conditions of the CCM (Figure 33a) and the real conditions from the calibrated numerical model (Figure 33b). The main difference is that the displacement distribution is strongly affected by the vertical component, and not the radial deformations as assumed in the CCM curves.

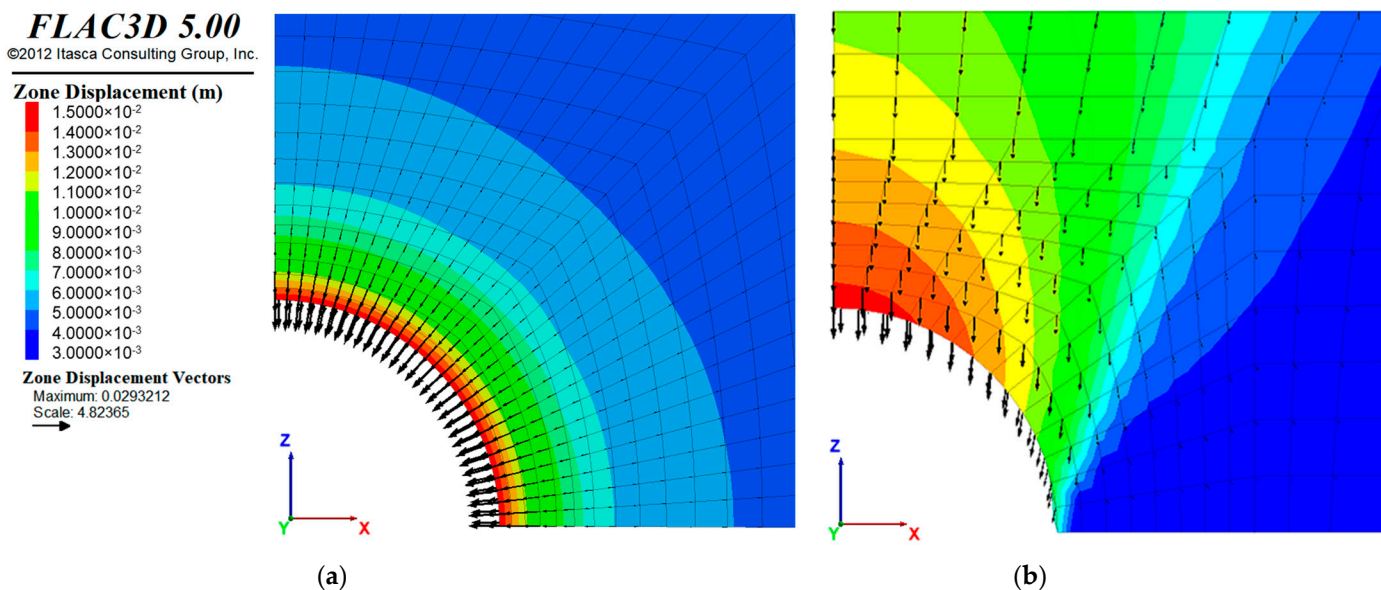


Figure 33. Displacement contours around the tunnel calculated with (a) the idealized conditions of the analytical methods, and (b) real conditions of the calibrated numerical model.

6. Optimization of Tunnel Lining Performance

In order to study the sensitivity of the primary and secondary lining thickness on the tunnel performance, a parametric analysis was conducted. Four different cases were considered, as summarized in Table 4. The lining performance was established based on interaction diagrams [29,50,51], comparing the computed bending moment and the normal force (M-N) combination with the limit defined by the boundary in the interaction diagram. These diagrams are a simplified graphical representation of the critical fault surface, separating acceptable load combinations and those that exceed the allowed limits. The σ - ϵ method was used to derive the M-N interaction diagrams (i.e., bending moment–normal force) [51,52]. Figures 34a and 34b show the constitutive model considered for the secondary lining (i.e., concrete and steel bars, respectively), and Figure 34c, the constitutive model for the primary lining (i.e., shotcrete reinforced with steel fibers), where the contribution of the steel fibers in the tension portion of the curve can be seen.

Table 4. Cases of primary lining thickness analyzed.

Case	Primary Lining Thickness (m)	Secondary Lining Thickness (m)
1	0.2	0.4
2	0.3	0.3
3	0.4	0.2
4	0.6	---

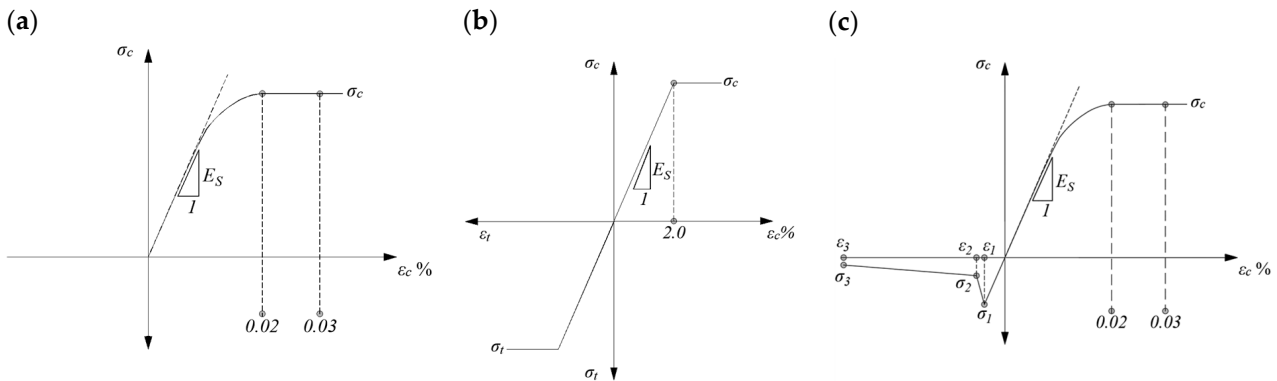


Figure 34. Constitutive laws used in the definition of interaction diagrams: (a) concrete, (b) steel bars, and (c) steel fiber-reinforced shotcrete (SFRS).

Figure 35a,b shows the interaction diagrams and acting forces on the first three cases, on the primary and secondary linings, respectively. In all cases, the acting forces on the secondary lining are minimal and are concentrated in the center of the diagram. On the other hand, the acting forces on the primary lining are more important; nevertheless, they still have a good safety factor gap, which is more evident in the case with the primary lining thickness of 60 cm (Figure 36). In addition, Figure 37 shows the surface vertical displacement profiles in a cross-section perpendicular to the tunnel axis, from all the studied cases. As expected, with the primary lining thickness of 60 cm, the magnitude of settlements is minor even without the secondary lining, which in this case has a negligible contribution. These results suggest that the best alternative for tunneling in these types of materials is the use of only one robust lining, because it can support the forces from the ground stress redistribution during tunneling while decreasing the impact of the excavation on the surface. Such an alternative has been used in past tunnel projects in nearby zones with similar geotechnical conditions [47], and around the, highlighting its rapid construction as well as its practical installation compared to a composite lining. Although several problems have been identified in the usage of single linings, like high temperatures during strength gaining, high deformation, and shrinkage, it has been observed that these limitations can be overcome if the lining is sprayed in two to three layers.

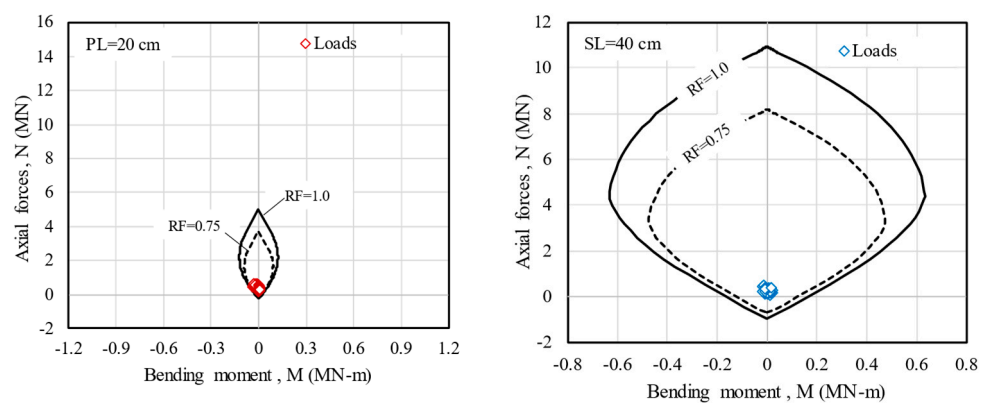


Figure 35. Cont.

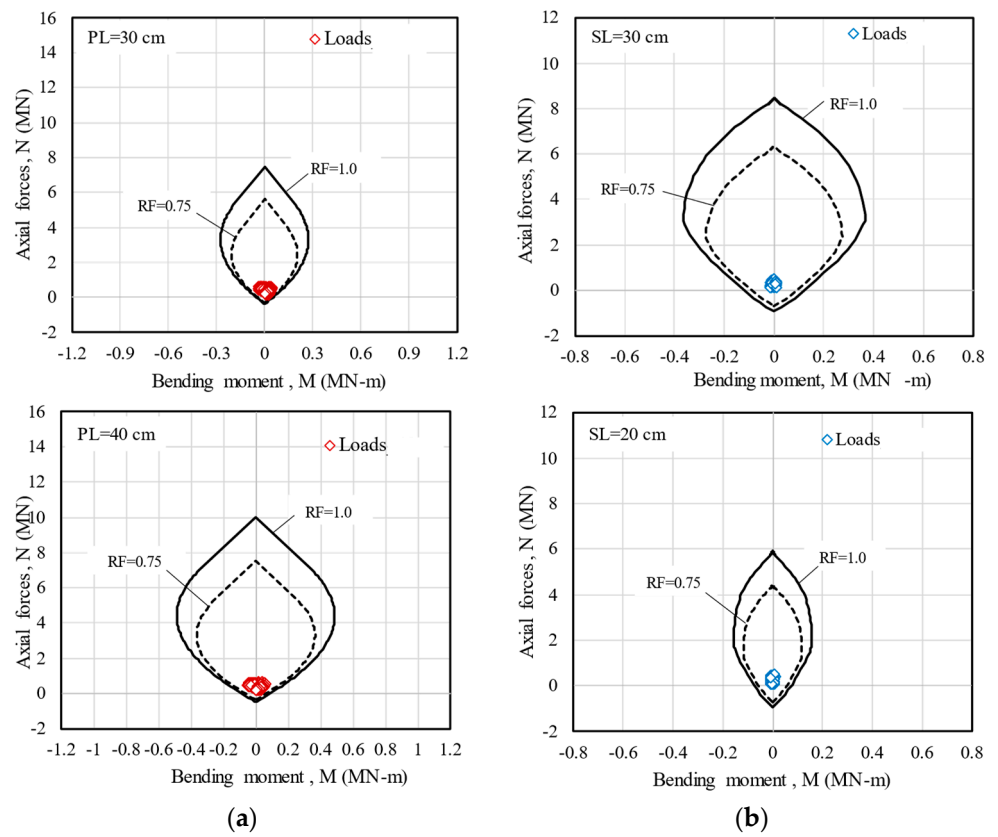


Figure 35. Interaction diagrams and acting loads at (a) the primary lining and (b) secondary lining.

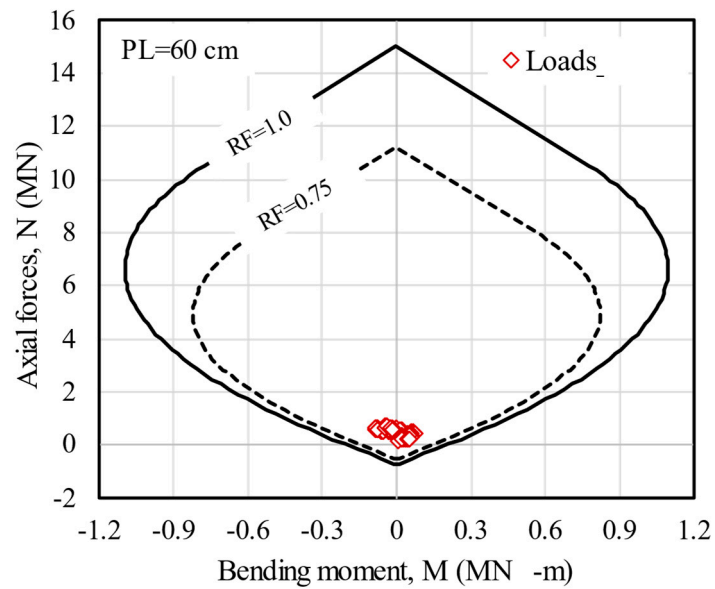


Figure 36. Interaction diagram and acting loads at primary lining.

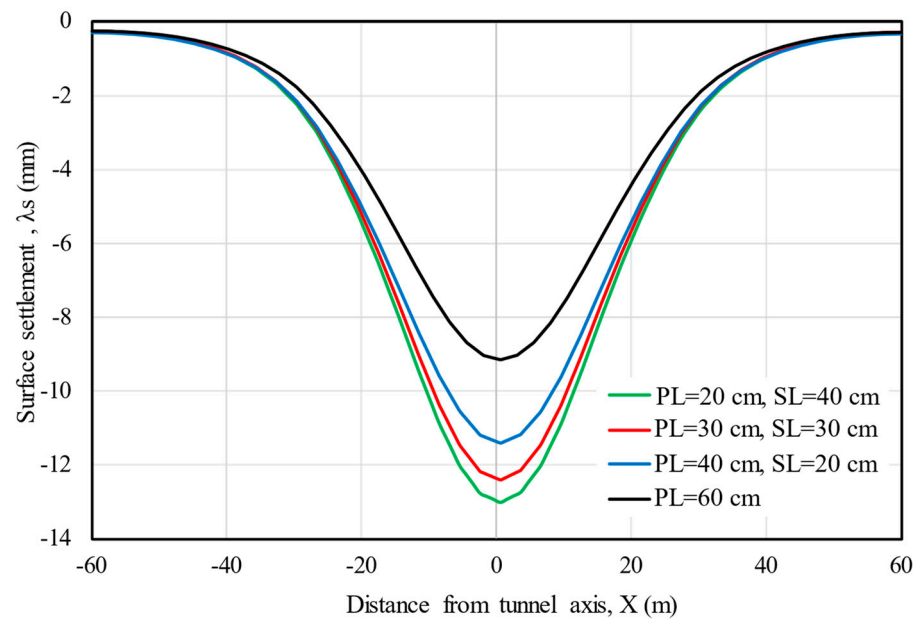


Figure 37. Surface vertical displacements perpendicular to the tunnel axis for each case analyzed.

7. Conclusions

Modern tunnel lining design must include the revision of state limits of failure and service simultaneously using a performance-based design approach. In urban areas, this is a key step to effectively reduce ground movement of the tunnel's surrounding soil, which, in turn, can lead to differential settlements on adjacent structures, and potential structural damage. This paper aims to partially fill the gap in field data regarding the load distribution acting on primary linings during conventional tunneling. An extensive instrumentation of a section of a tunnel of a 4.5 km long metro currently under construction in the north-western area of Mexico City was carried out. The instrumentation comprised load cells to measure radial and axial pressures in the primary lining, an extensometer, topographical survey points at the ground surface, and convergence and divergence readings of the tunnel cross-section. The presented results are further analyzed with three-dimensional finite difference numerical models. From both experimental and numerical data gathered, it can be clearly seen that the traditional analytical models substantially underpredict both ground deformations as well as design loads in the primary lining. This is most likely due to the hypothesis employed to derive these analytical solutions, such as circular tunnel cross-section and uniform isotropic stress field, among others. It is important to highlight that in the horseshoe tunnel geometry studied here, the displacement distribution is strongly affected by the vertical component, and not by radial deformations as assumed in the CCM approaches revised. Therefore, the lining performance design following these procedures is not optimal and can potentially lead to unsafe and costly designs, and in extreme cases, damage to surrounding structures. Special care should be exercised in brittle soils, such as cemented sandy silts and silty sands, which exhibit a strain softening behavior, and in which the failure surface is reached at relatively small ground deformations, precluding catastrophic collapses. Underprediction of the equilibrium tunnel crown vertical deformation on the order of one-third of the measured deformation was observed. Loads inferred in the secondary lining based on the back-calibrated numerical model are almost one-tenth of those taken by the primary lining. This fact can be attributed to the brittleness of the cemented silty sands, which leads to the fact that approximately 70 to 90% of the soil load is taken by the primary lining during the initial excavation advance, prior to the construction of the secondary lining. Thus, from the numerical study presented here, it can be concluded that it is more efficient in urban populated areas, when using the conventional tunneling method in stiff cemented soils, to have a robust lining that allows better control of the ground deformation, less detrimental impact in adjacent structures, and

faster construction than a support comprising primary and secondary linings. Therefore, one robust lining can support the surrounding soil loads, redistribute the soil stresses around the tunnel during excavation, and decrease the impact on the surface. Both state limits of failure and service are to be revised during the design phase. Using empirical and analytical approaches should be restricted to preliminary estimations.

Some of the limitations and uncertainties that could be considered in the present research are as follows:

1. Instrumentation: The complexity during the installation of the instruments can affect the accuracy of the data obtained, as well as soil heterogeneities which lead to an irregular contact surface between the load cell and the adjacent soil.
2. Single control section: Only one control section was instrumented. Ideally, two or three additional sections should have been installed to compare the results among several cases and observe the tunnel performance under different geotechnical conditions and tunnel coverages for a better generalization of the results.
3. Surface loads: The consideration of loads due to traffic on the roadways, especially in the tunnel sections with low cover, can influence the final conclusions.
4. External factors: Aspects such as climate conditions, groundwater, and seismic loading were not considered in this study.

Author Contributions: Conceptualization, J.M.M. and J.F.S.-F.; methodology, J.M.M. and J.F.S.-F.; writing—original draft, J.M.M. and J.F.S.-F. All authors have read and agreed to the published version of the manuscript.

Funding: This research has been funded by the Institute of Engineering at National Autonomous University of Mexico. Grant number R73.

Institutional Review Board Statement: Not applicable.

Informed Consent Statement: Not applicable.

Data Availability Statement: The raw data supporting the conclusions of this article will be made available by the authors on request.

Conflicts of Interest: The authors declare no conflicts of interest.

References

1. Mayoral, J.M. Performance evaluation of tunnels built in rigid soils. *Tunn. Undergr. Space Technol.* **2014**, *43*, 1–10. [[CrossRef](#)]
2. Mayoral, J.M.; Melis-Maynar, M.J.I.; de la Sancha, A.R. Integral Approach of Performance-Based Design for Tunnels. *Transp. Res. Rec. J. Transp. Res. Board* **2015**, *2522*, 121–130. [[CrossRef](#)]
3. de Ágreda, E.A.P. Failures Inspire Progress: Protecting Sensitive Buildings from Tunnelling. *GeoStrata Mag. Arch.* **2019**, *23*, 34–39. [[CrossRef](#)]
4. Oliver, A. Heathrow trial runs under question. *New Civil Engineer*. 3 November 1994; 4–5.
5. Oliver, A. Rush to stabilise Heathrow chasm. *Int. J. Rock Mech. Min. Sci. Geomech. Abstr.* **1995**, *4*, 189A.
6. Sousa, R.L.; Einstein, H.H. Lessons from accidents during tunnel construction. *Tunn. Undergr. Space Technol.* **2021**, *113*, 103916. [[CrossRef](#)]
7. Dong, Z.; Zhang, X.; Tong, C.; Chen, X.; Feng, H.; Zhang, S. Grouting-induced ground heave and building damage in tunnel construction: A case study of Shenzhen metro. *Undergr. Space* **2022**, *7*, 1175–1191. [[CrossRef](#)]
8. Lim, C.X.; Jusoh, S.N.; Lim, C.B.; Abdullah, R.A.; Yunus, N.Z.M. Tunnel depth effect to pile in Tunnel's influence zone. *Phys. Chem. Earth* **2023**, *129*, 103298. [[CrossRef](#)]
9. Son, M. Response analysis of nearby structures to tunneling-induced ground movements in sandy soils. *Tunn. Undergr. Space Technol.* **2015**, *48*, 156–169. [[CrossRef](#)]
10. Son, M. Response analysis of nearby structures to tunneling-induced ground movements in clay soils. *Tunn. Undergr. Space Technol.* **2016**, *56*, 90–104. [[CrossRef](#)]
11. ITA. *General Report on Conventional Tunnelling Method*; International Tunnelling and Underground Space Association: Chatelaine-Geneve, Switzerland, 2009; p. 27.
12. Behnen, G.; Nevrly, T.; Fischer, O. Soil-structure interaction in tunnel lining analyses. *Geotechnik* **2015**, *38*, 96–106. [[CrossRef](#)]
13. Bierbaumer, A.H. *Die Dimensionierung Des Tunnel Manerwerks*; W. Engelmann: Liepzig, Germany, 1913.
14. Szechy, K. *The Art of Tunnelling*; Akademiai Kaido: Budapest, Hungary, 1970.

15. Terzaghi, K. *Introduction to Tunnel Geology in Rock Tunneling Withsteel Supports*; The Commercial Shearing and Stamping Co.: Youngstown, OH, USA, 1964.
16. Bin, L.; Liu, X.; Xu, M. Reliability Analysis of Primary Supports in Deep and Soft-rock Tunnel Based on Probabilistic Design Numerical Method. *Electron. J. Geotech. Eng.* **2016**, *21*, 5013–5028.
17. Einstein, H.H.; Schwartz, C.W. Simplified Analysis for Tunnel Support. *J. Geotech. Eng. Div.* **1979**, *105*, 499–518. [[CrossRef](#)]
18. Ghorbani, A.; Hasanzadehshooiili, H. A comprehensive solution for the calculation of ground reaction curve in the crown and sidewalls of circular tunnels in the elastic-plastic-EDZ rock mass considering strain softening. *Tunn. Undergr. Space Technol.* **2019**, *84*, 413–431. [[CrossRef](#)]
19. Oreste, P. The convergence-confinement method: Roles and limits in modern geomechanical tunnel design. *Am. J. Appl. Sci.* **2009**, *6*, 757–771. [[CrossRef](#)]
20. Panet, M.; Bouvard, A.; Dardard, B.; Dubois, P.; Givet, O.; Guilloux, A.; Launay, J.; Duc, N.M.; Piraud, J.; Tournery, H.; et al. *The Convergence-Confinement Method AFTES—Recommendations des Groupes Travail*; French Association of Tunnels and Underground Space (AFTES): Paris, France, 2001.
21. Oreste, P.P. A Procedure for Determining the Reaction Curve of Shotcrete Lining Considering Transient Conditions. *Rock Mech. Rock Eng.* **2003**, *36*, 209–236. [[CrossRef](#)]
22. Verman, M.; Singh, B.; Jethwa, J.L.; Viladkar, M.N. Determination of Support Reaction Curve for Steel-Supported Tunnels. *Tunn. Undergr. Space Technol.* **1995**, *10*, 217–224. [[CrossRef](#)]
23. Wang, Y.Q.; Luo, M.R. Analysis of Support Reaction Curves considering Time-Varying Effect of Shotcrete. *Adv. Civ. Eng.* **2020**, *2020*, 6069432. [[CrossRef](#)]
24. Sadeghiyan, R.; Hashemi, M.; Moloudi, E. Determination of longitudinal convergence profile considering effect of soil strength parameters. *Int. J. Rock Mech. Min. Sci.* **2016**, *82*, 10–21. [[CrossRef](#)]
25. Vlachopoulos, N.; Diederichs, M.S. Improved Longitudinal Displacement Profiles for Convergence Confinement Analysis of Deep Tunnels. *Rock Mech. Rock Eng.* **2009**, *42*, 131–146. [[CrossRef](#)]
26. Argyroudis, S.; Tsiniadis, G.; Gatti, F.; Ptilakis, K. Effects of SSI and lining corrosion on the seismic vulnerability of shallow circular tunnels. *Soil Dyn. Earthq. Eng.* **2017**, *98*, 244–256. [[CrossRef](#)]
27. Guo, X.; Du, D.; Dias, D. Reliability analysis of tunnel lining considering soil spatial variability. *Eng. Struct.* **2019**, *196*, 11. [[CrossRef](#)]
28. Hamrouni, A.; Dias, D.; Sbartai, B. Reliability analysis of shallow tunnels using the response surface methodology. *Undergr. Sp.* **2017**, *2*, 246–258. [[CrossRef](#)]
29. Mayoral, J.M.; Mosqueda, G.; De La Rosa, D.; Alcaraz, M. Tunnel performance during the Puebla-Mexico 19 September 2017 earthquake. *Earthq. Spectra* **2020**, *36*, 288–313. [[CrossRef](#)]
30. Mayoral, J.M.; Mosqueda, G. Foundation enhancement for reducing tunnel-building seismic interaction on soft clay. *Tunn. Undergr. Space Technol.* **2021**, *115*, 104016. [[CrossRef](#)]
31. Panet, M.; Guenot, A. Analysis of convergence behind the face of a tunnel: Tunnelling 82. In Proceedings of the 3rd International Symposium, Brighton, UK, 7–11 June 1982; International Journal of Rock Mechanics and Mining Sciences & Geomechanics Abstracts; IMM: London, UK, 1982; Volume 20, pp. 197–204.
32. Ptilakis, K.; Tsiniadis, G.; Leanza, A.; Maugeri, M. Seismic behaviour of circular tunnels accounting for above ground structures interaction effects. *Soil Dyn. Earthq. Eng.* **2014**, *67*, 1–15. [[CrossRef](#)]
33. Wood, D.M. *Geotechnical Modelling*; Taylor y Francis; CRC Press: Boca Raton, FL, USA, 2004.
34. He, B.M.; Zhang, X.W.; Li, H.P. Ground load on tunnels built using new Austrian tunneling method: Study of a tunnel passing through highly weathered sandstone. *Bull. Eng. Geol. Environ.* **2019**, *78*, 6221–6234. [[CrossRef](#)]
35. Karakus, M.; Fowell, R.J. Back analysis for tunnelling induced ground movements and stress redistribution. *Tunn. Undergr. Space Technol.* **2005**, *20*, 514–524. [[CrossRef](#)]
36. Zhang, D.; Fang, Q.; Li, P.; Wong, L.N.Y. Structural Responses of Secondary Lining of High-Speed Railway Tunnel Excavated in Loess Ground. *Adv. Struct. Eng.* **2013**, *16*, 1371–1379. [[CrossRef](#)]
37. Ng, C.W.W.; Lu, H.; Peng, S.Y. Three-dimensional centrifuge modelling of the effects of twin tunnelling on an existing pile. *Tunn. Undergr. Space Technol.* **2013**, *35*, 189–199. [[CrossRef](#)]
38. Nomoto, T.; Imamura, S.; Hagiwara, T.; Kusakabe, O.; Fujii, N. Shield Tunnel Construction in Centrifuge. *J. Geotech. Geoenvironmental Eng.* **1999**, *125*, 237–345. [[CrossRef](#)]
39. Song, G.; Arshall, A.M. Centrifuge modelling of tunnelling induced ground displacements: Pressure and displacement control tunnels. *Tunn. Undergr. Space Technol.* **2020**, *103*, 103461. [[CrossRef](#)]
40. Mayoral, J.M.; Alcaraz, M.; Tepalcapa, S. Seismic performance of soil–tunnel–building systems in stiff soils. *Earthq. Spectra* **2023**, *39*, 1214–1239. [[CrossRef](#)]
41. Hettiarachchi, H.; Brown, T. Use of SPT Blow Counts to Estimate Shear Strength Properties of Soils: Energy Balance Approach. *J. Geotechnical Geoenvironmental Eng.* **2009**, *135*, 830–834. [[CrossRef](#)]
42. American Association of State Highway and Transportation Officials (AASHTO). *LRFD Bridge Design Specifications*; AASHTO: Washington, DC, USA, 2012.
43. Itasca Consulting Group. *FLAC, Fast Lagrangian Analysis of Continua. User's Guide*; Itasca Consulting Group, Inc.: Minneapolis, MN, USA, 2009.

44. Panet, M. *Calcul des Tunnels par la Méthode de Convergence—Confinement*; Presses de l'École Nationale des Ponts et Chaussées: Paris, France, 1995; p. 178.
45. Alonso, E.; Alejano, L.R.; Varas, F.; Fdez-Manin, G.; Carranza-Torres, C. Ground response curves for rock masses exhibiting strain-softening behavior. *Int. J. Numer. Anal. Methods Geomech.* **2003**, *27*, 1153–1185. [[CrossRef](#)]
46. Stille, H.; Holmberg, M.; Nord, G. Support of weak rock with grouted bolts and shotcrete. *Internatinal J. Rock Mech. Min. Sci.* **1989**, *26*, 99–113. [[CrossRef](#)]
47. Tamez, E.; Rangel, J.L.; Y Holguin, E. *Diseño Geotécnico de Túneles*; TGC Geotecnia: Mexico City, Mexico, 1997. (In Spanish)
48. Fairhurst, C. General philosophy of support design for underground structures in hard rock. *Undergr. Struct. Des. Constr.* **1991**, *59*, 1–55.
49. Chern, J.C.; Shiao, F.Y.; Yu, C.W. *An Empirical Safety Criterion for Tunnel Construction: Proceedings of the Regional Symposium on Sedimentary Rock Engineering*; Public Construction Commission: Taipei, Taiwan, 1998; pp. 222–227.
50. Kaiser, P. Rational assessment of tunnel liner capacity. In *Proceedings of the 5th Canadian Tunneling Conference*, Montreal, QC, Canada; 1985.
51. Sauer, G.; Gall, V.; Bauer, E.; Dietmaier, P. Design of tunnel concrete linings using limit capacity curves. In *Proceedings of the 8th International Conference on Computer Methods and Advances in Geomechanics*, Morgantown, WV, USA, 22–28 May 1994; pp. 2621–2626.
52. Vandewalle, L. Recommendations of RILEM TC 162-TDF: Test and design methods for steel fibre reinforced concrete. *Mater. Struct. Mater. Constr.* **2000**, *33*, 3–5.

Disclaimer/Publisher's Note: The statements, opinions and data contained in all publications are solely those of the individual author(s) and contributor(s) and not of MDPI and/or the editor(s). MDPI and/or the editor(s) disclaim responsibility for any injury to people or property resulting from any ideas, methods, instructions or products referred to in the content.